



# Influence of mechanical activation on crystal structure and physical properties of $\text{YbFeO}_3$

Zhengyou Li<sup>1</sup> · Kamaludin Abdulvakhidov<sup>1</sup> · Bashir Abdulvakhidov<sup>2</sup> · Alexander Soldatov<sup>1</sup> · Alexander Nazarenko<sup>3</sup> · Pavel Plyaka<sup>3</sup> · Aram Manukyan<sup>4</sup> · V. Jagadeesha Angadi<sup>5</sup> · Svetlana Shapovalova<sup>1</sup> · Marina Sirota<sup>1</sup> · Marina Vitchenko<sup>6</sup> · Irina Mardasova<sup>6</sup> · Elza Ubushaeva<sup>7</sup> · Suleiman Kallaev<sup>8</sup> · Zairbek Omarov<sup>8</sup>

Received: 9 August 2022 / Accepted: 9 November 2022

© The Author(s), under exclusive licence to Springer-Verlag GmbH, DE part of Springer Nature 2022

## Abstract

In this work, the influence of simultaneous action of high pressure and shear deformation (mechanical activation) on the physical properties of synthesized  $\text{YbFeO}_3$  was studied using complex methods. The formation of crystalline structures of  $\text{YbFeO}_3$  powders with different concentrations of structural defects was carried out using Bridgman anvils. It was found that during mechanical activation, the tilting angles of  $\text{FeO}_6$  oxygen octahedra change within the range  $\theta = 12.69\text{--}28.45^\circ$ . Using X-ray diffraction, it was established that the linear unit cell parameters  $a$ ,  $b$  and  $c$  change in a consistent manner with changing mechanical activation pressure, while the space-group symmetry  $D_{2h}^{16}\text{-}Pbnm$  is preserved. The sizes of the coherent scattering regions ( $D$ ) decrease by more than 90% at the maximum mechanical activation pressure (1200 MPa). It was found that the mechanical activation pressures of  $\text{YbFeO}_3$  have a threshold value (800 MPa), above which the dislocation density decreases. According to the results of impedance spectroscopy, the nature of relaxation was found to be non-Debye and the activation energy increased from 0.649 eV for the starting sample to 1.395 eV for the sample mechanically activated sample at 1 GPa. The magnetization curves  $M(H)$  were described using the law of approach to magnetic saturation (LAS), and the critical crystallite size ( $D_{cr}$ ) was determined to be 50 nm, at which the maximum  $H_c$  is observed. The behaviors of the spectroscopic splitting factor ( $g$ ) and half-width ( $\Delta H$ ) of the electron paramagnetic resonance (EPR) spectrum are analogous to  $H_c$  and  $M_r$ , however, the maximum  $\Delta H$  is observed in the range of 50–105 nm, and the  $g$ -factor reaches its maximum at particle sizes of 105 nm.

**Keywords** Orthoferrite · Mechanical activation · Impedance · Magnetization · EPR

✉ Kamaludin Abdulvakhidov  
phys.kam@mail.ru

<sup>1</sup> Southern Federal University, Sladkova 178/24, Rostov-On-Don, Russia 344090

<sup>2</sup> Dagestan State University, Gadgieva 43-a, Makhachkala, Russia 367000

<sup>3</sup> Southern Scientific Center of the Russian Academy of Sciences, Chekhova 41, Rostov-On-Don, Russia 344006

<sup>4</sup> Institute for Physical Research, NAS of Armenia, Ashtarak, 378410 Yerevan, Armenia

<sup>5</sup> P.C. Jabin Science College, Hubballi 580031, India

<sup>6</sup> Don State Technical University, Gagarin Sq. 1, Rostov-On-Don, Russia 344000

<sup>7</sup> Moscow Aviation Institute, Volokolamskoe Shosse, 4, Moscow, Russia 125993

<sup>8</sup> Dagestan Federal Research Centre of the Russian Academy of Sciences, Makhachkala, Russia 532096

## 1 Introduction

Perovskite structure of orthoferrites  $\text{RFeO}_3$ , where  $\text{R}$  is a rare-earth element or yttrium, has recently attracted significant attention due to their unique properties and potential applications as smart devices, sensors for gas detection, oxygen-permeable membranes, active catalysts for oxidation or reduction of pollutant gases, as electrode materials in solid oxide fuel cells, next-generation spintronics and memory devices [1–8].

Like all orthoferrites, the rare-earth multiferroic  $\text{YbFeO}_3$  is characterized by weak ferromagnetism at high temperatures, which is due to the non-collinear spin arrangement of iron ions ( $\text{Fe}^{3+}$ ). The rare-earth ions  $\text{R}$  are in a disordered paramagnetic state in the voids among  $\text{FeO}_6$  oxygen octahedra. The crystal structures of these compounds have been studied in detail by Marezio and

Dernier [9]. The crystal symmetry of  $\text{RFeO}_3$  orthoferrites coincides with the magnetic one and is described by the orthorhombic space group  $D_{2h}^{16}$ - $Pbnm$ . The unit cell contains four iron ions and four rare-earth ions. The cell exhibits a distortion associated with the tilts of the  $\text{FeO}_6$  octahedra around the orthorhombic axes  $b$  and  $c$  [10]. It was shown in [11] that the spin-reorientation transition takes place in the  $ac$  plane. These tilts lead to a deviation of the Fe–O–Fe bonds from  $180^\circ$ . Due to the Dzyaloshinskii–Moriya interaction [12] and the rotation of the  $\text{FeO}_6$  octahedron, it has been experimentally confirmed that  $\text{RFeO}_3$  orthoferrites have an antiferromagnetic configuration and macroscopic magnetism [13].  $\text{RFeO}_3$  systems have two sorts of magnetic sub-lattices: the  $3d$ -electron of the Fe sub-lattice and  $4f$ -electron of the R sub-lattice, as well as three different superexchange interactions  $\text{Fe}^{3+}-\text{Fe}^{3+}$ ,  $\text{R}^{3+}-\text{R}^{3+}$  and  $\text{Fe}^{3+}-\text{R}^{3+}$  that determine their magnetic properties at different temperatures and external fields [14].

Upon cooling to 600–700 K from higher temperatures corresponding to the paramagnetic state,  $\text{RFeO}_3$  transforms into an antiferromagnetically ordered state. The antiferromagnetic ordering temperature  $T_N$  for different  $\text{RFeO}_3$  is different and increases with increasing ionic radius  $r$  [15, 16]. Therefore,  $\text{LaFeO}_3$  has the highest Néel temperature  $T_N$  (740 K), while  $\text{LuFeO}_3$  has the lowest (623 K). According to [16],  $\text{YbFeO}_3$  has a temperature  $T_N=627$  K. The interaction between the  $\text{Fe}^{3+}$  and  $\text{R}^{3+}$  sub-lattices determines many static and dynamic properties, as well as spin-orientation phase transitions of the first and second order.

During the first-order spin-orientation transitions, the ordering parameter  $\theta$ , which is the angle of rotation of the magnetic moment with respect to the crystal axes  $b$  and  $c$ , changes abruptly. According to [17], this angle directly determines the distance between oxygen  $2p$ -orbitals and iron  $3d$ -orbitals, which are responsible for the electrical and optical properties. In most orthoferrites, second-order transitions are associated with the continuous rotation of the weak ferromagnetic moment of the  $\text{Fe}^{3+}$  sub-lattices and the induced moment in the  $\text{R}^{3+}$  subsystem. In both cases of phase transition, the magnetic symmetry changes abruptly at the transition point [18]. The onset and completion of a spontaneous orientational phase transition occur at temperatures  $T_1$  and  $T_2$ , which are the second-order phase transition temperatures. The canted phase exists in a narrow range  $T_1-T_2$  and for  $\text{YbFeO}_3$ ,  $T_1=7.95$  and  $T_2=6.80$  K [19]. Another direct evidence that spontaneous reorientation occurs via two second-order phase transitions is provided by the data on the heat capacity measurements obtained for  $\text{YbFeO}_3$ . In this case, jumps in the heat capacity were also observed at temperatures of the beginning  $T_1$  and ending  $T_2$  of the spin-reorientation process, indicating the presence of

second-order phase transitions [18]. The magnetic groups and spin configurations of orthoferrites are given in [20].

An analysis of the literature sources, including those cited above, shows that they are mainly devoted to studying the low-temperature properties of rare-earth orthoferrites. However, the most demanded functional devices are those that operate at room temperature and higher temperatures. Therefore, this work aims to study the possibility of controlling the physical properties of  $\text{YbFeO}_3$ , which is characterized by its antiferromagnetic phase at room and high temperatures.

## 2 Materials and methods

Phase pure  $\text{YbFeO}_3$  composition was obtained via solid-state reaction method in a previous work [21]. The starting materials,  $\text{Yb}_2\text{O}_3$  (Sigma-Aldrich,  $\geq 99.9\%$ ) and  $\text{Fe}_2\text{O}_3$  (Sigma-Aldrich,  $\geq 99.9\%$ ), were premixed according to the stoichiometric ratio. The mixture was ground manually for 2 h with Diamonite mortar and pestle in the presence of ethanol, which reduce its particle size and improve its homogeneity. The resulting mixture was dried in a thermostat at 200 °C to remove moisture. Then, the dried mixture was again ground to achieve even finer particle size. This fine powder was palletized into pellets, put in a platinum crucible, and sintered in a furnace at 1200 °C for 14 h in an air atmosphere. After which the furnace was turned off and cooled by inertia to room temperature. The synthesized  $\text{YbFeO}_3$  was ground into powder and studied on a Bruker D2 Phaser (Germany) diffractometer using  $\text{Cu K}_\alpha$  radiation with a step  $\Delta 2\theta=0.01^\circ$  and a data acquisition time  $\tau=0.1$  s per step. Then, equal-weight portions of the  $\text{YbFeO}_3$  powder were mechanically activated between Bridgman anvils at various pressures. The lower anvil rotated at a speed of 3 rpm. The number of revolutions for each sample was two. The parameter  $\zeta$ , characterizing the shear deformation was determined to equal 12 by the formula [22]:

$$\zeta = \ln\left(\frac{vr}{d}\right), \quad (1)$$

where  $v$  is the rotation angle,  $r$  is the radius of the anvil, and  $d$  is the thickness of the sample.

Furthermore, the crystal structure of the starting and mechanically activated powders was investigated by full-profile Rietveld analysis of powder diffraction data at room temperature.

From seven equal-weight portions of  $\text{YbFeO}_3$  powder mechanically activated at the same pressure, a sample with a diameter of 10 mm and a thickness of about 1 mm was pressed at a pressure of 2 kN for subsequent sintering of the ceramic. Ten such samples mechanically activated at various pressures were prepared. All these samples were sintered together at 900 °C for 2 h. Depending on the pressure of

the mechanical activation, the density of ceramic samples ranges from 6.65 to 7.10 g/cm<sup>3</sup>. For impedance measurements, silver electrodes were deposited on both faces of the sample by a silver paste coating, which was dried at 750 °C for 10 min. Optical absorption spectra were measured using a double-beam UV–Visible spectrophotometer (Shimadzu Double Beam UV-2600, Japan) at room temperature. The microstructure of the samples was observed and examined by a scanning electron microscope (LEO EVO 40 XVP; Carl Zeiss AG, Germany). The magnetic properties of samples were measured on a vibrating sample magnetometer (VSM, LakeShore 7404, USA) at room temperature. Impedance spectroscopy at high temperatures was measured using a PARSTAT 4000 system (Princeton Applied Research, USA). Electron paramagnetic resonance (EPR) spectra were studied using an X-band spectrometer at a frequency of 9.36 GHz.

### 3 Results and discussion

#### 3.1 Structural characterization

Electron micrographs of the starting and mechanically activated at 900 MPa are shown in Fig. 1a and Fig. 1b, respectively. The insets show enlarged parts of the selected area. A characteristic feature of all samples after mechanical activation is the presence of many non-isometric particles, which in turn are agglomerations of smaller particles. Due to the different concentrations of structural defects in each sample, they are also in different metastable states. This means that when ceramics are sintered from such powders, their activation energies of diffusion processes are different and unambiguously lower than that of the non-activated powder.

These diffraction profiles were further refined using Rietveld refinement via Powder Cell 2.4 software [23] and were found to fit in orthorhombic syngony with the space group  $D_{2h}^{16}$ -Pbnm. Rietveld refinement plots with refinement goodness

parameters of the starting and all the mechanically activated YbFeO<sub>3</sub> powders are shown in Supplementary Figs. S1–S10. Figure 2a and Fig. 2b show some of the diffraction profiles, the selected angular interval and the half width at half maximum of the (112) peak, demonstrating the shift of the Bragg profiles as a function of mechanical activation pressure.

As compared to the starting sample, with increasing pressure, the Bragg profiles of mechanically activated samples are smeared, the integrated intensity decreases and the diffuse background increases. This behavior is due to structural changes in powders during mechanical activation, which we will describe in more detail below.

The average coherent scattering regions ( $D$ ) and microstrains ( $\Delta d/d$ ) were calculated using the Williamson–Hall plot.

$$\beta_{(hkl)} \cdot \cos(\theta) = (\Delta d/d) \cdot (4\sin(\theta)) + k\lambda/D, \quad (2)$$

where  $D$  – the average coherent scattering region,  $\Delta d/d$  – microstrain. Figure 3 shows plots of  $4\sin(\theta)$  as a function of  $\beta_{(hkl)} \cdot \cos(\theta)$ , where  $\beta_{(hkl)}$  is the true half-width.

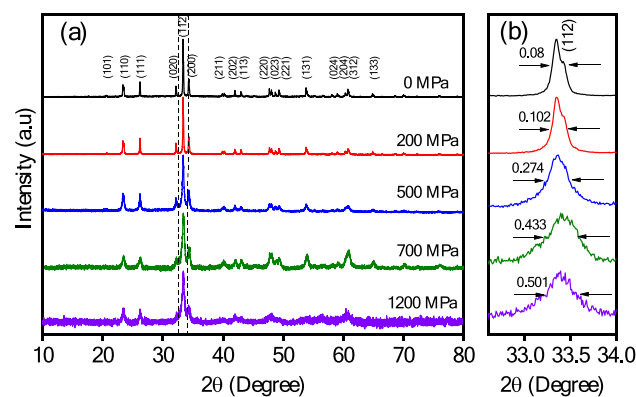


**Fig. 2** Rietveld refinement plots of starting and mechanically activated YbFeO<sub>3</sub> powders (a), the selected angular interval (b)

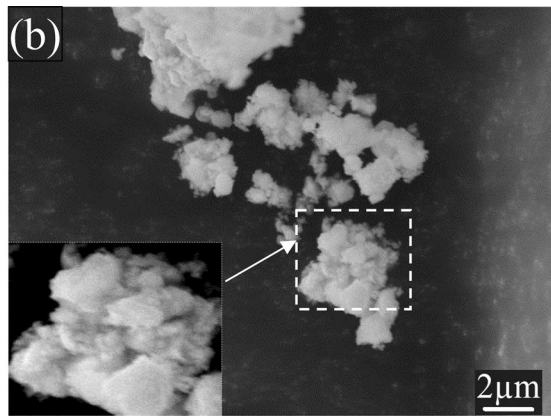
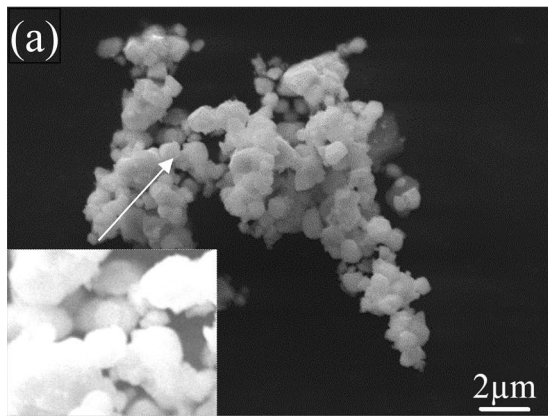


**Fig. 1** Electron micrographs of starting (a) and mechanically activated YbFeO<sub>3</sub> powder samples at a pressure of 900 MPa (b)

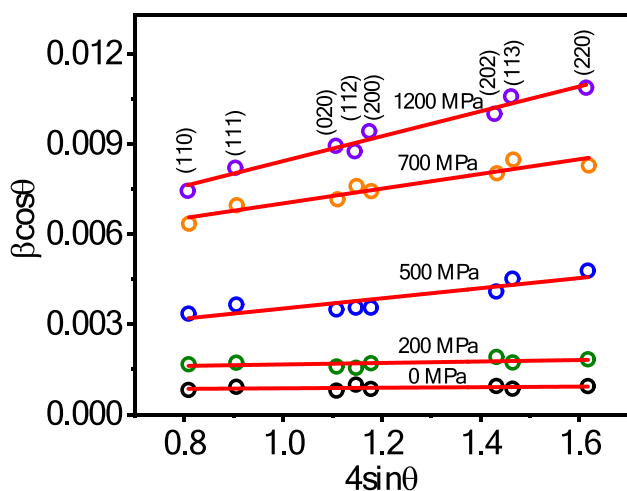


**Fig. 3** Williamson–Hall plots for starting and mechanical activated  $\text{YbFeO}_3$  samples at various pressures

Let us consider the behavior of the linear unit cell parameters  $a$ ,  $b$ , and  $c$  calculated from the diffraction profiles. Figure 4a shows the dependencies of these parameters on the mechanical activation pressure. A characteristic feature of all these parameters is their coherence, but non-monotonic change with a change in the pressure of mechanical activation.

All the unit cell parameters show a dip at about 700 MPa is due to ballistic diffusion, where the mechanically activated powder recrystallizes and turns into a hard crystalline disk, whose parameters practically approach those of the single-crystal sample studied in [14]. Mechanical activation at pressures of 900 and 1100 MPa is accompanied by some increase in  $D$  and a decrease in  $\Delta d/d$  (see Fig. 4b). Such a situation occurs during dynamic recrystallization. The recrystallization process is characterized by the migration of point defects, the “healing” of some dislocations, and a change in the unit cell parameters [24–26]. The dislocation density was calculated as in [27, 28] using the formula:

$$\rho_D = 3nD^{-2}, \quad (3)$$

where  $n = 1$ ,  $D$  – the average size of coherent scattering regions.

The results of the calculations are given in Table 1.

It is known that the smaller  $\Delta d/d$  and the larger  $D$ , the more perfect the crystal structure is, however, changes in the linear parameters of the unit cell cannot be explained solely by the changes in the concentrations of dislocations and point defects. The main distortions of the ideal perovskite structure in orthoferrites can be attributed to rotations of oxygen octahedra relative to the central  $\text{Fe}^{3+}$  ions and slight deformations of the octahedra as well as displacements of  $\text{R}^{3+}$  ions in the  $ab$ -plane [29].

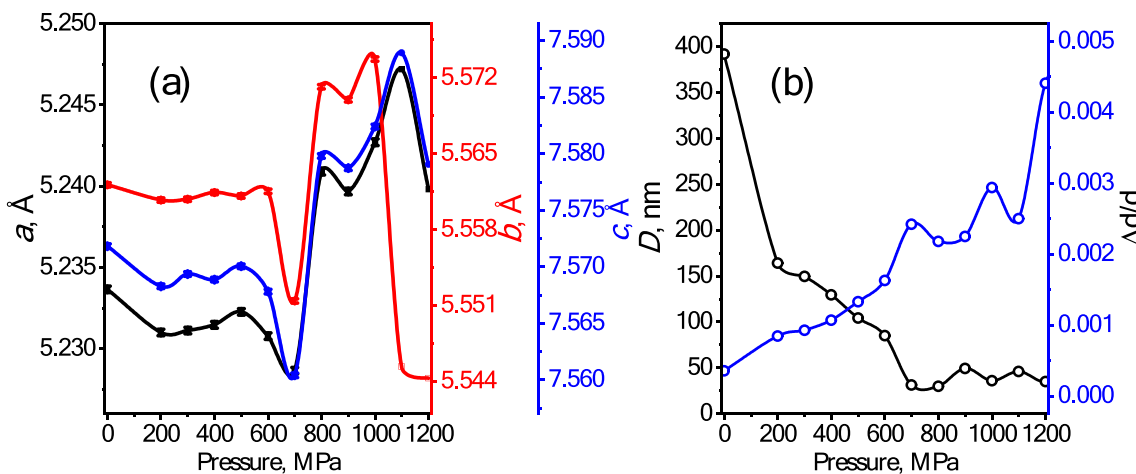


**Fig. 4** Dependencies of unit cell parameters (a), sizes of coherent scattering regions  $D$  and microstrains  $\Delta d/d$  (b) on the pressure of mechanical activation

**Table 1** Dislocation densities of  $\text{YbFeO}_3$

P, MPa	0	200	300	400	500	650
$\rho_D \cdot 10^9, \text{cm}^{-2}$	2	11	13	18	28	41
P, MPa	700	800	900	1000	1100	1200
$\rho_D \cdot 10^9, \text{cm}^{-2}$	303	337	123	231	141	245

Since mechanical activation is a process of mechanical force action with the relaxation of mechanical energy via various channels [22, 30], the crystal lattice must undergo noticeable distortions and transition to a metastable state. We visualized the structure of YbFeO<sub>3</sub> after mechanical activation at various pressures with the VESTA 3 program [31], and monitored the behavior of the tilt and rotation angle and bond lengths in FeO<sub>6</sub> oxygen octahedra with the Powder Cell 2.4 software. Figures 5a–c show models of such distorted structures and the starting sample.

The data on tilt angles and bond lengths for FeO<sub>6</sub> oxygen octahedra are given in Table 2, from which it is easy to see that all of these quantities change significantly with increasing mechanical activation pressure. Literature data for the tilt angle  $\theta = (180 - \angle \text{Fe-O}_1\text{-Fe})/2$  is equal to 19° [13]. The  $\theta$  values obtained by us are in the range of 18.85–24.4°. The values of the rotation angle  $\varphi = (90 - \angle \text{O-O-O})/2$  between adjacent octahedral were calculated according to [11], as shown in Table 2. Distortions (collapse) of FeO<sub>6</sub> oxygen octahedron and YbO<sub>8</sub> dodecahedron (changes in the tilt angles and bond lengths) should in turn affect the electrical, vibrational, and magnetic properties of YbFeO<sub>3</sub>, which we will discuss in more detail in the following sections.

### 3.2 Impedance spectroscopy

The method of impedance spectroscopy belongs to the group of relaxation methods, which are based on studying the response of a physical system to very weak external influences [21]. Impedance ( $Z^*$ ) is defined as the total resistance of a device to the AC flow at a given frequency and is expressed as a complex number. The total complex resistance (impedance) can be written as:

$$Z^* = Z' - j \cdot Z'', \quad (4)$$

**Table 2** The octahedral tilting angle  $\theta$ , rotation angle  $\varphi$ , and bond lengths

P, MPa	$\theta$ , °	$\varphi$ , °	Fe-O <sub>2</sub> , Å	Fe-O <sub>3</sub> , Å	Fe-O <sub>1</sub> , Å
0	18.88	11.9	2.024	2.004	2.002
200	18.87	12.4	2.034	1.983	2.002
300	18.85	10.3	2.035	1.955	2.002
400	19.88	12.4	2.024	1.984	2.012
500	19.95	13.8	2.054	1.964	2.023
600	18.87	12.4	2.091	1.961	2.014
700	20.33	3.3	2.375	1.496	2.023
800	23.97	2.5	2.054	1.964	2.022
900	20.42	7.2	2.083	1.833	2.081
1000	12.69	9.6	2.041	1.891	2.022
1100	28.45	7.5	2.006	1.950	2.051
1200	22.58	1.7	2.315	1.915	2.061

where  $Z'$  is the active (real) and  $Z''$  is the reactive (imaginary) component.

Figures 6a–d shows the Cole–Cole diagrams of the complex impedance  $Z^*$  of the starting and mechanically activated YbFeO<sub>3</sub> samples at various pressures. The  $Z^*$  measurements were carried out at various temperatures and frequencies. All Cole–Cole diagrams are characterized by approximately equally stretched arcs at room temperatures, which turn into semicircles with increasing temperature.

Generally, the number of semicircles corresponds to different relaxation processes due to grains and grain boundaries and/or coexisting phases. In our case, no additional semicircle was observed, indicating the absence of a specific grain boundary phase. As the temperature increases, the diameter of the semicircle decreases, therefore the impedance decreases. This indicates a characteristic feature of the thermally activated conduction process. The centers of the semicircles are located below the real axis, which corresponds to the non-Debye type of relaxation.

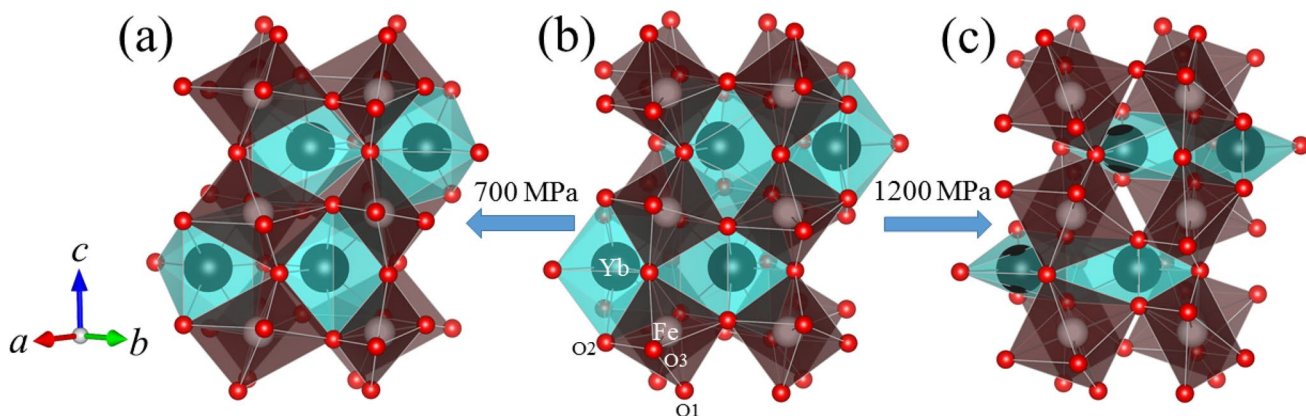


**Fig. 5** Model representation of structural changes in YbFeO<sub>3</sub> orthoferrite at a pressure of 700 MPa (a), 0 MPa (b) and 1200 MPa (c)

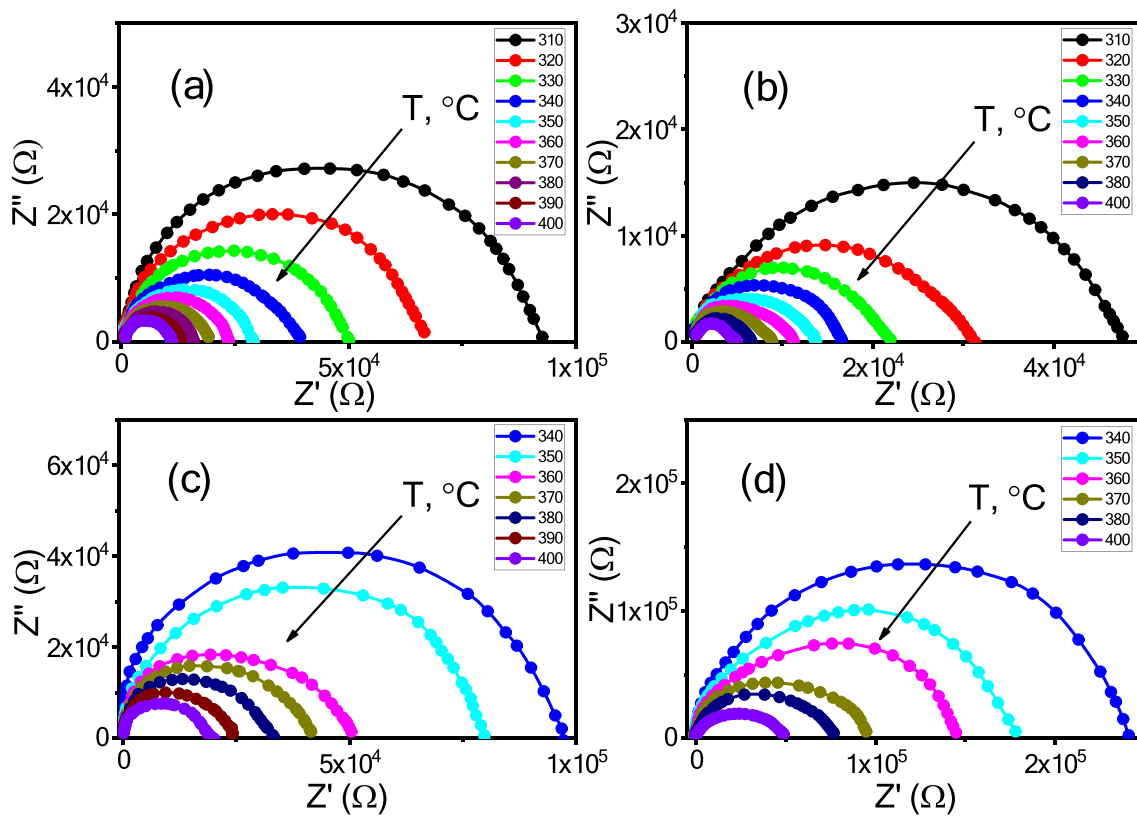


**Fig. 6** Cole–Cole diagrams of starting (a) and mechanical activated  $\text{YbFeO}_3$  samples at pressures of 200 (b), 500 (c), and 1000 MPa (d)

Figures 7a–d and a'–d'' show the change of  $Z'$  and  $Z''$  as a function of frequency and temperature of the starting and activated samples at pressures of 200, 500, and 1000 MPa, respectively. As shown in Fig. 7a–d,  $Z'$  has higher values at low frequencies, decreases monotonically with increasing frequency, and merges at higher frequencies ( $\sim 1$  MHz) regardless of temperature. For the sample activated at a pressure of 200 MPa,  $Z'$  decreases compared to the starting sample. According to the intensities of the diffraction profiles for this sample, an increase in the degree of its mosaicity was observed compared to the starting sample. Usually, an increase in the degree of mosaicity is observed during the deformation or dispersion of the samples under small mechanical force actions [32]. When sintering ceramics from mechanically activated powders, some of the dislocations are retained, and some of them are "healed". It is known that the effective diffusion coefficient of charge carriers is different along and across the dislocation "tube"; along the "tube" increases many times, and across decreases. Possibly, for this reason,  $Z'$  of a sample mechanically activated at 200 MPa with a low dislocation concentration decreases after mechanical activation. However, for samples that are mechanically activated at higher pressures, dislocation concentrations increase (see Table 1), and the values of  $Z'$  increase many-fold due to the anisotropic nature of

the charge carriers scattering by dislocations. Also, in this case, charge transfer between the electrodes is difficult. Here and below, to compare  $Z'$ , we have taken the temperature  $T = 350$   ${}^\circ\text{C}$  in the paramagnetic phase, where there are no processes associated with the phase transition, as the reference temperature.

A decrease in  $Z'$  with increasing temperature and frequency is a general trend for all samples and is due to an increase in AC conductivity. As shown in Figs. 7a–d, in the high-frequency region, all curves merge regardless of temperature, indicating a possible release of the space charge and a consequent lowering of the barrier properties of materials [33].

Figure 7a'–d' shows the frequency dependencies of the imaginary part of the impedance  $Z''$  of the same samples. The peak value  $Z''_{\max}$  of each sample is suppressed with increasing temperature and shifted to higher frequencies. For a sample activated at a pressure of 200 MPa, the frequency  $f_{\max}$ , corresponding to the peak value of  $Z''_{\max}$ , increases by more than three times, but  $Z''_{\max}$  had the smallest value among all samples. With increasing temperature, the peaks broaden and shift toward higher frequencies, indicating a thermally activated relaxation phenomenon that is temperature-dependent. The relaxation time ( $\tau$ ) also decreases with increasing frequency and temperature. The source of the

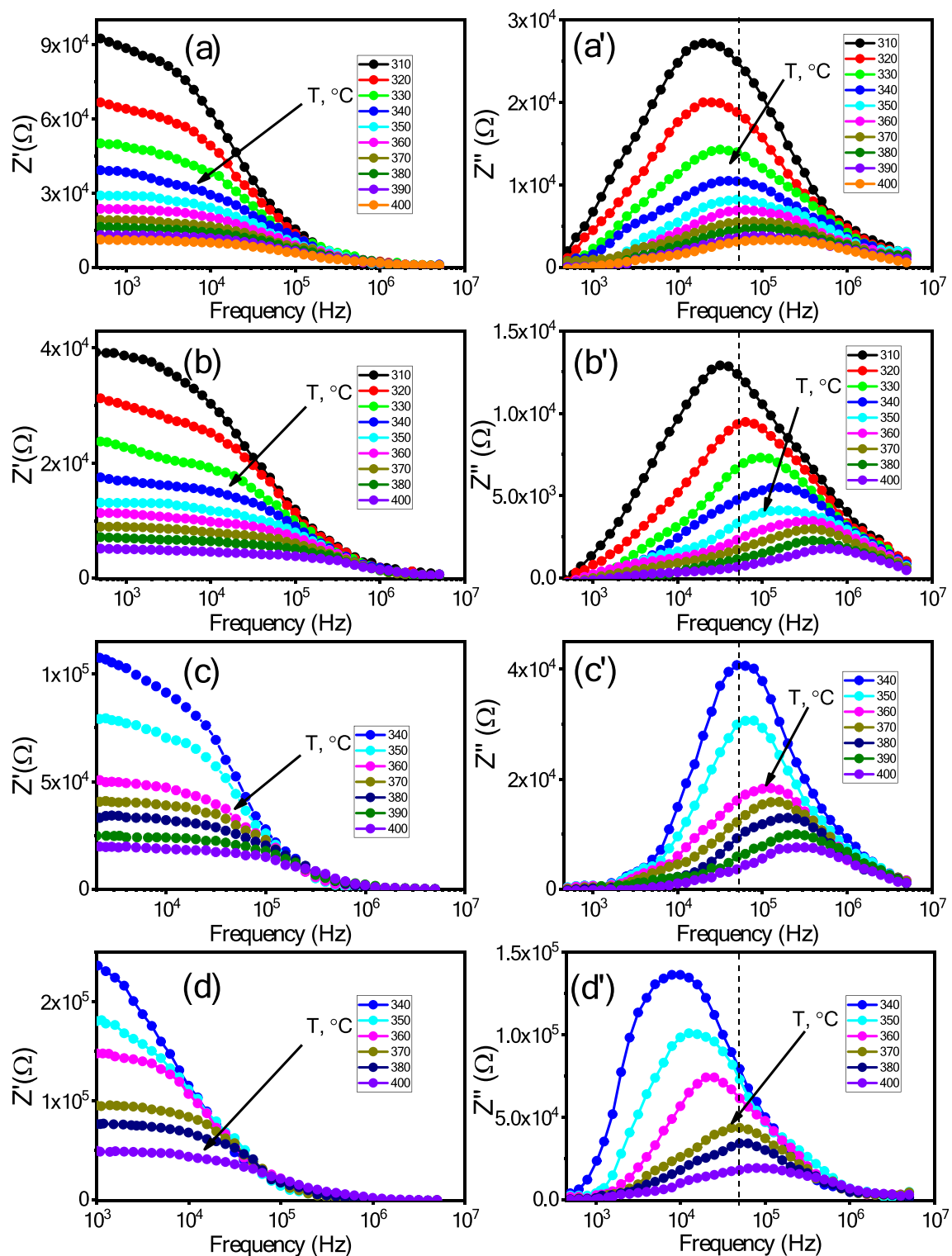


**Fig. 7** Frequency-temperature dependencies of the real and imaginary parts of the impedance  $Z^*$  of starting (a) and mechanically activated YbFeO<sub>3</sub> ceramics at a pressure of 200 (b), 500 (c), and 1000 MPa (d)

(d). The vertical dash line corresponds to the  $Z''_{\max}$  of the starting sample at 350 °C

relaxation behavior can be space charges accumulated both at the boundaries of structural inhomogeneities of crystallites (dislocations) resulting from mechanical activation and Schottky defects. The latter is known to be weakly bound to the crystal lattice and can easily migrate across the surface of crystallites.

The value of grain resistance ( $R_g$ ) for each temperature is determined by the intersection of the corresponding semicircle with the frequency axis. Grain capacity ( $C_g$ ) is calculated using  $R_g$  and  $f_{\max}$  of the semicircle from the equation [33]:

$$2\pi f_{\max} R_g C_g = 1. \quad (5)$$

The values of these quantities at  $T=350$  °C are given in Table 3.

A comparison of the  $R_g$  and  $C_g$  values of ceramics obtained before and after mechanical activation of powders shows that with increasing mechanical activation pressure,

$C_g$  tends to decrease, while  $R_g$  changes nonmonotonically but it is larger (except for a pressure of 200 MPa) than the starting sample.

Since the relaxation of the impedance of the studied compositions is a thermally activated process, we calculated the activation energy based on the experimental data of the relaxation time using the Arrhenius equation:

$$\tau = \tau_0 \exp \frac{E_a}{k_B T}, \quad (6)$$

where  $\tau_0$  – pre-exponential factor,  $E_a$  – activation energy,  $k_B$  – Boltzmann constant and  $T$  – absolute temperature. The results obtained are shown in Fig. 8a–d. Here, a significant increase in  $E_a$  with an increase in the mechanical activation pressure is clearly visible.

### 3.3 Magnetic properties

#### 3.3.1 Magnetic hysteresis loops

Previously, in [14, 24], we presented the results of studying the influence of mechanical activation on the magnetic properties of  $\text{Er}_3\text{Fe}_5\text{O}_{12}$  and  $\text{Yb}_3\text{Fe}_5\text{O}_{12}$  and found that parameters such as coercive force ( $H_c$ ), saturation magnetization ( $M_s$ ), remanent magnetization ( $M_r$ ) depend on

**Table 3** Dependencies of the capacitance and resistance of  $\text{YbFeO}_3$  ceramics on the mechanical activation pressure of powders

P, MPa	0	200	500	1000
$R_g$ , Ohm	28,860	13,663	79,500	178,000
$C_g$ , nF	0.105	0.062	0.029	0.057

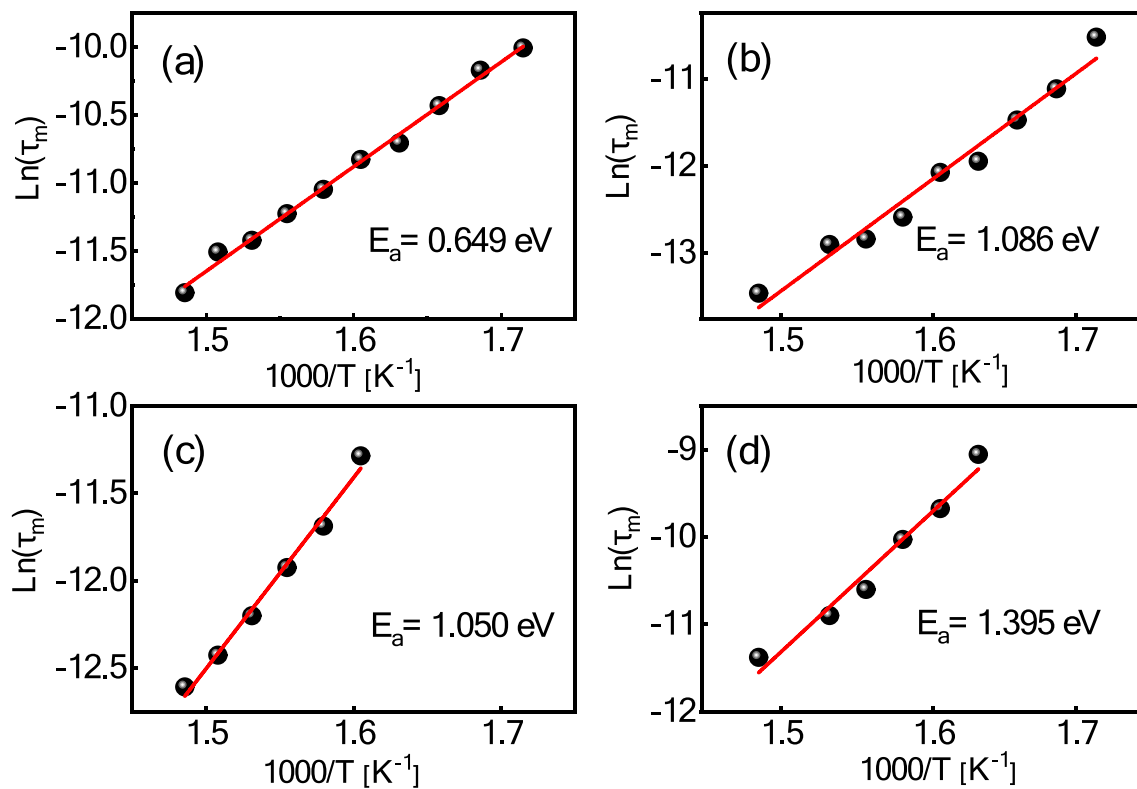


**Fig. 8** Activation energy of starting (a) and mechanically activated  $\text{YbFeO}_3$  at a pressure of 200 MPa (b), 500 MPa (c), and 1000 MPa (d)

the shape, the random orientation crystallographic axes, the presence of defects in the crystal lattice, and grain sizes  $2R_c$  (clusters). Since we are talking about nanoscale objects, below the grain sizes, we refer to the  $D$  sizes. Since the mechanical activation of magnetic crystalline bodies is a process of accumulation of structural defects and mechanical stresses in crystallites with subsequent dispersion of the latter, in them a stochastic (random) magnetic structure with an inhomogeneous distribution of magnetization is formed. In this case, the magnetic order is preserved at lengths  $R_L > R_C$ . Therefore, the model of random magnetic anisotropy is used to study the structure–property correlation, which assumes that the axes of easy magnetization in individual crystallites (clusters) are randomly oriented [34]. The random orientation of the crystallographic axes leads to the formation of a fluctuating local anisotropy in space. For most uniaxial polycrystals with randomly oriented axes of easy magnetization in crystallites in the region of strong magnetic fields, the magnetization curve can be described by the law of approach to magnetic saturation (LAS) [35–37]:

$$\frac{M(H)}{M_s} = M_s \left[ 1 - \frac{1}{2} \left( \frac{a^{1/2} H_a}{H} \right)^2 \right], \quad (7)$$

where  $a^{1/2} H_a$  – the root-mean-square fluctuation of the effective local anisotropy field (within the radius  $R_c$ ),  $a$  – the dispersion of the anisotropy axes, equal to 1/15 for randomly oriented uniaxial anisotropy axes. The occurrence of the coefficient 1/2 is due to the “internal” magnetic field, which is caused by the different orientations of the magnetization vectors of different grains and is necessary for measurements in fields  $H < < 4\pi M_s$  [38].

However, Eq. (7) does not fit the  $M(H)$  curve of YbFeO<sub>3</sub> in magnetic fields above 2 kOe (see Fig. 9a, inset in the

left corner). For approximation, the formula suggested in [39] has turned out to be the most suitable:

$$M = M_s \left( 1 - \frac{1}{15} \frac{H_A^2}{H^{1/2} (H^{3/2} + H_R^{3/2})} \right) + \chi H, \quad (8)$$

where  $H_R$  is the exchange field,  $\chi H$  is the high-field paramagnetic response (often called the so-called paramagnetism-like term) [40–42]. In high fields,  $\chi H$  makes a fairly significant contribution to  $M(H)$ , which grows linearly with increasing magnetic field  $H$ . As can be seen from the inset in the lower right corner of Fig. 9a, YbFeO<sub>3</sub> is a soft magnetic composition with a coercive field  $H_c < 100$  Oe.

Domain displacement occurs at magnetic fields smaller than  $H_c$ , and the order of fields  $H_c$  is also sufficient for the irreversible rotation of magnetic moments. Therefore, choosing the most appropriate approximation function and selecting the fitting parameters are important. Based on these considerations, we chose the lower field threshold to 200 Oe, and the upper one to 2 kOe, and fitted the law of approach to magnetic saturation for five samples (see Fig. 9b).

Curve fitting of experimental data was performed using NLSF in Origin [39]. The values of the statistical fitting parameters  $k^2$  and  $R^2$  for all samples are given in Table 4, and the microscopic parameters obtained from the fit are given in Table 5.

The effective local anisotropy constant of the samples was calculated using the formula:

$$K_{\text{eff}} = \frac{H_a M_s}{2}. \quad (9)$$

Now, let us consider the dependence of the main parameters of the magnetic hysteresis loop on the  $D$  size. According to the classical concepts [43], the value of  $H_c$  is determined by the energy of motion resistance of the

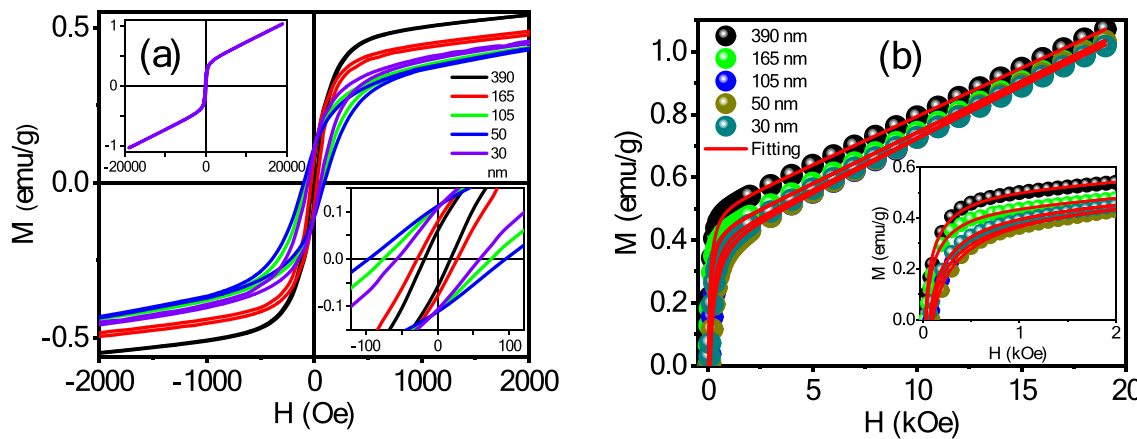


**Fig. 9** Magnetic hysteresis loops (a) and fit to the law of approach to magnetic saturation (b) for YbFeO<sub>3</sub>

**Table 4** Values of fitting parameters  $k^2$  and  $R^2$  for  $\text{YbFeO}_3$  samples

$2R_c$ , nm	30	50	105	165	390
$k^2 \times 10^{-5}$	1.68	8.37	2.16	10.1	18.2
$R^2$	0.99997	0.99988	0.99996	0.99981	0.99966

**Table 5** Dependence of the values of the parameters of the stochastic domains on the sizes of crystallites

$2R_c$ , nm	30	50	105	165	390
$H_a$ , Oe	1410	1182	1646	860	883
$M_s$ , emu/g	0.395	0.383	0.378	0.417	0.485
$H_R$ , Oe	621	788	723	414	455
$\chi$ , $10^{-5}$ emu/(g·Oe)	3.299	3.431	3.453	3.255	3.086
$K_{\text{eff}}$ , J/m <sup>3</sup>	233.4	187.9	258.7	149.8	178.7

domain wall, and starting from  $\sim 0.1\text{--}1\ \mu\text{m}$ , decreases with increasing the grain size. In this case, the magnetization process is determined by the magnetocrystalline anisotropy of individual grains. The relationship between  $H_c$  and  $D$  can be represented by the following expression:

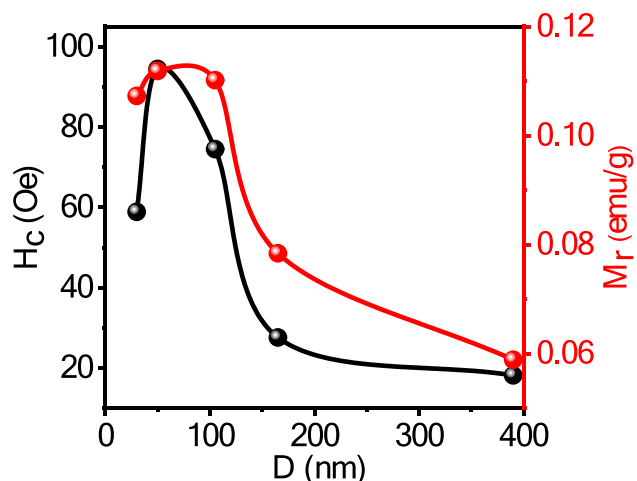
$$H_c \sim D^{-n}, \quad (10)$$

where  $n$  is theoretically any positive number.

For  $\text{YbFeO}_3$ , an increase in  $H_c$  on going to  $D_{\text{cr}}$  (50 nm) is due to a change in the magnetization reversal mechanism, i.e., a transition from the displacement of domain walls to the coherent rotation of the magnetic moment. With a further decrease the size of particles ( $D < D_{\text{cr}}$ ) to a single domain state, the value of  $H_c$  decreases [44]. The dependence looks like this:

$$H_c \sim D^n. \quad (11)$$

This is possible due to the existence of an intergrain ferromagnetic exchange interaction, which occurs when the grain size  $D$  is smaller than the exchange interaction length  $L_{\text{ex}}$  [45]. At a sufficiently small nanograin size, the role of local magnetic anisotropy sharply decreases: the averaged magnetic anisotropy  $\langle K \rangle$  takes very small values, and magnetization reversal processes become less dependent on local magnetic anisotropy. This facilitates the process of magnetization. Such a dependence of  $H_c$  on  $D$  has been called the Heitzer diagram in the literature [46]. It allows one to determine the critical grain size  $D_{\text{cr}}$  ( $2R_c^*$ ). In our case, this parameter is equal to 50 nm. The  $M_r$  parameter practically repeats the evolution of  $H_c$  (see Fig. 10).

**Fig. 10** Size dependencies of the coercive field  $H_c$ , remanent magnetization  $M_r$ 

### 3.3.2 Paramagnetic resonance spectrum

Earlier, in [25], we presented the results of a study of the influence of mechanical force action on the electron paramagnetic spectra (EPR) of  $\text{Yb}_3\text{Fe}_5\text{O}_{12}$  and found a significant influence of mechanical pressure on the parameters of the EPR spectrum. In the present work, the goal is not to study in detail all the factors that lead to the broadening of the EPR spectra, hence we will focus on the role of crystallite sizes without forgetting the structural defects present in them [47].

Figure 11a shows the EPR spectra obtained after mechanical activation, and Fig. 11b shows the parameters of these spectra as a function of crystallite size. The spectroscopic splitting factor ( $g$ -factor) was calculated from the well-known formula:

$$g = \frac{hv}{\mu_B H_{\text{eff}}}, \quad (12)$$

where  $h$  - the Planck's constant,  $\mu_B$  - the Bohr magneton,  $H_{\text{eff}}$  - the magnitude of the effective magnetic field,  $\nu$  - the absorption frequency. The spectral lines are well described by Lorentz functions, and the half-width  $\Delta H$  was calculated as the "peak" – "peak" distance in Fig. 11a.

As shown in Fig. 11b, the  $g$ -factor of the starting sample (equal to 1.809) differs from the  $g$ -factor of free electrons.

A decrease in  $D$  size to 105 nm is accompanied by a monotonic increase in the  $g$ -factor from the initial value, while  $\Delta H$  also increases. However, a further decrease in the size  $D$  leads to a decrease in these values. Comparing these results with the results of the study on a vibration magnetometer shows that there is a size effect. However, it should also be considered that structural defects in

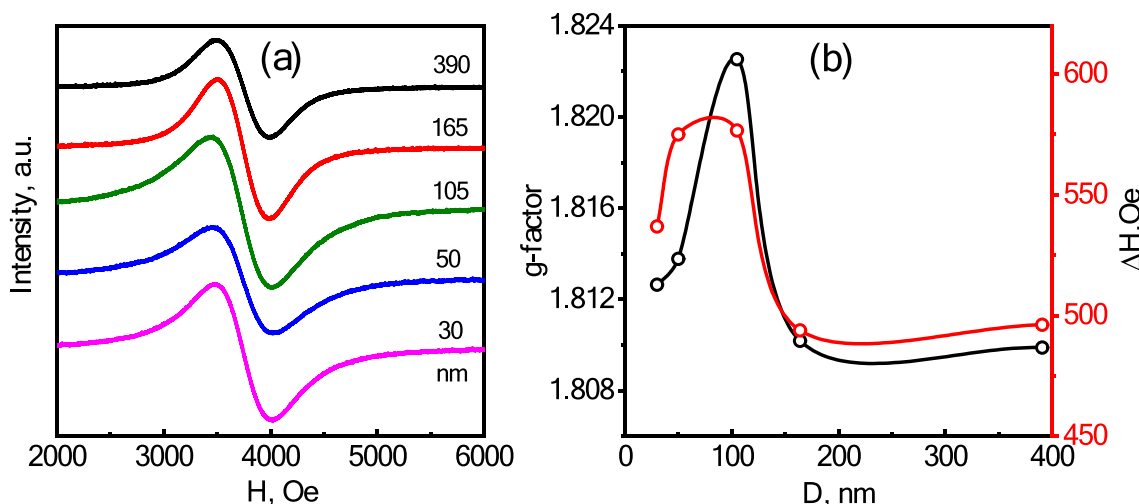


**Fig. 11** Size dependencies of the EPR spectra (a), g-factor and  $\Delta H$  (b)

ferromagnetic materials in field characteristic of reversible processes, e.g. the movement of domain walls, are stoppers and contribute to the value of  $H_c$ . In the field region where irreversible processes develop in a ferromagnet, dislocations and point defects can significantly reduce  $M_s$ .

## 4 Conclusion

In this work, the influence of mechanical activation and the resulting structural defects on the crystal structure and physical properties of the pre-synthesized YbFeO<sub>3</sub> powder was investigated for the first time at room and high temperatures. The tilt  $\theta$  and rotation angles  $\varphi$  of FeO<sub>6</sub> oxygen octahedra as well as the bond lengths and their dependence on the mechanical activation pressure were determined. It has been found that for YbFeO<sub>3</sub>, there is a mechanical activation threshold pressure of 800 MPa, at which the dislocation concentration reaches a maximum. Impedance spectroscopy has shown that the values of the complex components of ceramic samples sintered from mechanically activated samples depend on the mechanical activation pressure. An analysis of the magnetic hysteresis loops of YbFeO<sub>3</sub> powders shows that each loop is a combination of magnetic  $M(H)$  and paramagnetic  $\chi H$  components. By dispersing YbFeO<sub>3</sub> crystallites during mechanical activation, the critical size  $D_{cr}$  was found to be 50 nm, which corresponds to the maximum values of  $H_c$  and  $M_r$ . The parameters  $g$  and  $\Delta H$  of the EPR spectrum show similar behavior, the maximum  $\Delta H$  is observed in the range of 50–105 nm, and the g-factor reaches its maximum at particle sizes of 105 nm. Such a discrepancy may be due to various factors, among which it is worth mentioning a certain difference in the geometry of the experiment in the first (hysteresis loop) and in the second case, where the object

under study in the second case is located in the resonator and has the effect of a frequency of 9.36 GHz.

The set of experimental results obtained in the work allows us to conclude that it is possible to control the structural parameters and the desired physical properties of YbFeO<sub>3</sub> by the mechanical activation method at the technological level without changing the stoichiometry of the composition.

**Supplementary Information** The online version contains supplementary material available at <https://doi.org/10.1007/s00339-022-06235-z>.

**Acknowledgements** Research was financially supported by the Ministry of Science and Higher Education of the Russian Federation (State assignment in the field of scientific activity, No. 0852-2020-0019).

**Funding** Ministry of Science and Higher Education of the Russian Federation, 0852-2020-0019, Alexander Soldatov.

## Declarations

**Conflict of interest** The authors have no conflicts of interest to declare.

## References

1. H. Chen, G. Zhao, W. Fan, X. Ma, X. Luo, Y. Chen, B. Kang, Z. Feng, Z. Jin, S. Cao, Ceram. Int. **48**, 7564 (2022)
2. T. Inoue, N. Seki, K. Eguchi, H. Arai, J. Electrochem. Soc. **137**, 2523 (1990)
3. C. Alcock, R. Doshi, Y. Shen, Solid State Ionics **51**, 281 (1992)
4. J.G. McCarty, H. Wise, Catal. Today **8**, 231 (1990)
5. K. Tabata, M. Misono, Catal. Today **8**, 249 (1990)
6. N.Q. Minh, J. Am. Ceram. Soc. **76**, 563 (1993)
7. L.J.M.J. Blomen, M.N. Mugerwa, *Fuel Cell Systems* (Plenum Press, New York, 1993)
8. T. Yao, A. Ariyoshi, T. Inui, J. Am. Ceram. Soc. **80**, 2441 (2005)
9. M. Marezio, P.D. Dernier, Mater. Res. Bull. **6**, 23 (1971)

10. S.C. Parida, S.K. Rakshit, Z. Singh, J. Solid State Chem. **181**, 101 (2008)
11. Z.-Q. Wang, Y.-S. Lan, Z.-Y. Zeng, X.-R. Chen, Q.-F. Chen, Solid State Commun. **288**, 10 (2019)
12. A.V. Kimel, B.A. Ivanov, R.V. Pisarev, P.A. Usachev, A. Kirilyuk, T. Rasing, Nat. Phys. **5**, 727 (2009)
13. M.C. Weber, M. Guennou, H.J. Zhao, J. Íñiguez, R. Vilarinho, A. Almeida, J.A. Moreira, J. Kreisel, Phys. Rev. B **94**, 214103 (2016)
14. X. Ma, N. Yuan, X. Luo, Y. Chen, B. Kang, W. Ren, J. Zhang, S. Cao, Mater. Today Commun. **27**, 102438 (2021)
15. L. Sangaletti, L.E. Depero, B. Allieri, P. Nunziante, E. Traversa, J. Eur. Ceram. Soc. **21**, 719 (2001)
16. M. Eibschütz, S. Shtrikman, D. Treves, Phys. Rev. **156**, 562 (1967)
17. E. Haye, F. Capon, S. Barrat, P. Boulet, E. Andre, C. Carteret, S. Bruyere, J. Alloys Compd. **657**, 631 (2016)
18. K.P. Belov, A.K. Zvezdin, A.M. Kadomtseva, R.Z. Levitin, Sov. Phys. Uspekhi **19**, 574 (1976)
19. N.K. Danshin, S.V. Zherlitsyn, S.S. Zvada, G.G. Kramarchuk, M.A. Sdvizhkov, V.D. Fil, Sov. Phys. JETP **66**, 1227 (1987)
20. R.L. White, J. Appl. Phys. **40**, 1061 (1969)
21. O. Polat, M. Coskun, R. Kalousek, J. Zlamal, B. Zengin Kurt, Y. Caglar, M. Caglar, A. Turut, J. Phys. Condens. Matter. **32**, 065701 (2020)
22. R.Z. Valiev, I.V. Alexandrov, Nanostructured Mater. **12**, 35 (1999)
23. W. Kraus, G. Nolze, J. Appl. Crystallogr. **29**, 301 (1996)
24. K. Abdulvakhidov, A. Soldatov, I. Dmitrenko, Z. Li, S. Kallaev, Z. Omarov, Results Phys. **22**, 103905 (2021)
25. L. Zhengyou, K. Abdulvakhidov, A. Nazarenko, A. Soldatov, P. Plyaka, Y. Rusalev, A. Manukyan, I. Dmitrenko, M. Sirota, Appl. Phys. A **128**, 343 (2022)
26. K.G. Abdulvakhidov, M.A. Sirota, A.P. Budnyk, T.A. Lastovina, A.V. Soldatov, S.N. Kallayev, Z.M. Omarov, S.A. Sadykov, B.K. Abdulvakhidov, M.A. Vitchenko, I.V. Mardasova, P.S. Plyaka, R.G. Mitarov, Mater. Res. Express **5**, 115029 (2018)
27. M. Sirota, K. Abdulvakhidov, T. Lastovina, A. Pnevskaya, E. Ubushaeva, P. Plyaka, A. Nazarenko, M. Vitchenko, I. Mardasova, A. Budnyk, Phys. Status Solidi **218**, 2000782 (2021)
28. K.G. Abdulvakhidov, M.A. Sirota, A.P. Budnyk, T.A. Lastovina, B.K. Abdulvakhidov, S.A. Sadykov, P.S. Plyaka, A.V. Soldatov, J. Phys. Condens. Matter **31**, 135402 (2019)
29. A.S. Moskovin, D.G. Latypov, V.G. Gudkov, Phys. Solid State **30**, 413 (1988)
30. N.F. Uvarov, V.V. Boldyrev, Russ. Chem. Rev. **70**, 265 (2001)
31. K. Momma, F. Izumi, J. Appl. Crystallogr. **44**, 1272 (2011)
32. E.N. Ubushaeva, E.V. Likhushina, K.G. Abdulvakhidov, M.A. Vitchenko, B.K. Abdulvakhidov, V.B. Shirokov, N.V. Lyanguzov, Y.I. Yuzyuk, E.M. Kaidashev, I.V. Mardasova, Tech. Phys. Lett. **37**, 952 (2011)
33. I. Coondoo, N. Panwar, M.N.A. Rafiq, V.S. Puli, M.N.A. Rafiq, R.S. Katiyar, Ceram. Int. **40**, 9895 (2014)
34. G. Herzer, Acta Mater. **61**, 718 (2013)
35. R.S. Iskhakov, S.V. Komogortsev, Phys. Met. Metallogr. **112**, 666 (2011)
36. S.V. Komogortsev, R.S. Iskhakov, J. Magn. Magn. Mater. **440**, 213 (2017)
37. V.A. Ignatchenko, R.S. Iskhakov, G.V. Popov, Sov. J. Exp. Theor. Phys. **55**, 878 (1982)
38. S.V. Vonsovskii, Y.S. Shur, Ferromagnetism (Ferromagnetism). Moscow-Leningrad: OGIZ-Gostekhizdat (1948).
39. E.C. Devi, I. Soibam, J. Supercond. Nov. Magn. **32**, 1293 (2019)
40. H. Zhang, D. Zeng, Z. Liu, J. Magn. Magn. Mater. **322**, 2375 (2010)
41. B.D. Cullity, C.D. Graham, *Introduction to magnetic materials* (Wiley, New York, 2011)
42. T. Holstein, H. Primakoff, Phys. Rev. **58**, 1098 (1940)
43. R.M. Bozorth, *Ferromagnetism* (IEEE, New Jersey, 1993)
44. G.I. Frolov, O.I. Bachina, M.M. Zav'yalova, S.I. Ravochkin, M.M. Zav'yalova, S.I. Ravochkin, Tech. Phys. **53**, 1059 (2008)
45. G. Herzer, J. Magn. Magn. Mater. **112**, 258 (1992)
46. G. Herzer, *Handbook of magnetic materials* (Elsevier, Amstredam, 1997), pp.415–462
47. W. Low, F. Seitz, D. Turnbull, M. Sachs, Phys. Today **13**, 48 (1960)

**Publisher's Note** Springer Nature remains neutral with regard to jurisdictional claims in published maps and institutional affiliations.

Springer Nature or its licensor (e.g. a society or other partner) holds exclusive rights to this article under a publishing agreement with the author(s) or other rightsholder(s); author self-archiving of the accepted manuscript version of this article is solely governed by the terms of such publishing agreement and applicable law.